Electrochimica Acta 442 (2023) 141909

Contents lists available at ScienceDirect

Electrochimica Acta

journal homepage: www.journals.elsevier.com/electrochimica-acta

Nanostructured $Zn_xMn_{3-x}O_4$ thin films by pulsed laser deposition: A spectroscopic and electrochemical study towards the application in aqueous Zn-ion batteries

Andrea Macrelli [a,*], Marco Olivieri [a], Alessio Lamperti [b], Valeria Russo [a,c], Benedetto Bozzini [d], Marco Menegazzo [e], Gianlorenzo Bussetti [e], Carlo S. Casari [a,c], Andrea Li Bassi [a,c]

[a] Micro and Nanostructured Materials Lab (NanoLab), Department of Energy, Politecnico di Milano, Via G. Ponzio 34/3, 20133 Milano, Italy
[b] Institute for Microelectronics and Microsystems (IMM), Consiglio Nazionale delle Ricerche (CNR), Unit of Agrate Brianza, Via C. Olivetti 2, 20864 Agrate Brianza (MB), Italy
[c] Center for Nano Science and Technology (CNST), Instituto Italiano di Tecnologia (IIT), Via G. Pascoli 70/3, 20133 Milano, Italy
[d] Battery Materials Engineering Laboratory (BMEL), Department of Energy, Politecnico di Milano, Via G. La Masa 34, 20156 Milano, Italy
[e] Solid Liquid Interface Nano-Microscopy and Spectroscopy (SoLINano-Σ) lab, Department of Physics, Politecnico di Milano, Piazza Leonardo da Vinci 32, 20133 Milano, Italy

ARTICLE INFO

Keywords:
Pulsed laser deposition
Zinc-ion batteries
Nanostructured cathode materials
$ZnMn_2O_4$ thin films

ABSTRACT

Aqueous Zn-ion batteries (AZIBs) represent a safe and sustainable technology amongst the post-lithium systems, though the poor understanding of the material behaviour at the cathode prevents the full development of efficient AZIBs. $ZnMn_2O_4$ (ZMO) has been considered one of the cathode candidates owing to its analogy to the well-established $LiMn_2O_4$ cathode for lithium-ion batteries, however its electrochemical mechanism in the presence of Zn ions in aqueous environment is unclear and still debated. In this work, we synthesised nanostructured ZMO thin films by Pulsed Laser Deposition (PLD) and we evaluated, through extensive characterization by microscopic, spectroscopic, and diffraction techniques, how the deposition and annealing conditions affect the film properties. The self-supported nature and the high degree of control down to the nanoscale make a thin film an ideal model system to study the electrochemistry of the material in aqueous solution and to emphasize the impact of the film properties on its electrochemical response. We highlighted the crucial role of the oxygen pressure in the modulation of the film porosity and the combined effect of deposition pressure and annealing temperature to produce a film with tailored properties in terms of morphology, crystallinity, and Zn stoichiometry. A complex redox mechanism involving multiple concurrent reactions and the formation of zinc hydroxide sulphate hydrate (ZHS) was reported, as well as the influence of the film porosity on the voltammetric behaviour of the film at higher scan rate. Our results confirm the intricate electrochemical mechanism of the ZMO material, which does not merely involve the Zn^{2+} insertion/extraction but also the crucial participation of Mn^{2+} from the electrolyte, and pave the way for the nanoscale design of engineered ZMO-based electrodes.

1. Introduction

Rechargeable aqueous zinc-ion batteries (AZIBs) operating with a slightly acidic aqueous electrolyte and exploiting divalent Zn ions as charge carriers are a promising class of post-lithium next-generation batteries [1–3]. This type of secondary battery represents the evolution of primary alkaline zinc-ion batteries [4] and may be competitive against traditional lithium-ion batteries (LIBs) [5,6]. Indeed, zinc metal – notwithstanding shape-change and passivation issues that still have to be definitely sorted out [7–10] – can be effectively implemented as the anode and safely coupled with an aqueous medium, while lithium metal exhibits worse instability issues, combined with pyrophoricity [11]. Zinc metal is highly desirable due to its high theoretical gravimetric and volumetric specific capacities (820 mAh g^{-1} and 5850 mAh cm^{-3}, respectively), a redox potential of −0.76 V *vs.* SHE, and it can be produced and recycled using established processes [5]. Concerning the electrolyte, an aqueous medium is intrinsically safer and exhibits superior ionic conductivity compared to the flammable organic liquids

* Corresponding author.
E-mail address: andrea.macrelli@polimi.it (A. Macrelli).

https://doi.org/10.1016/j.electacta.2023.141909
Received 10 October 2022; Received in revised form 23 December 2022; Accepted 15 January 2023
Available online 16 January 2023

traditionally employed in the state-of-the-art LIBs [1,5].

Nevertheless, the bottleneck to the development of efficient rechargeable AZIBs is the cathode. A few material candidates are available to reversibly sustain several electrochemical cycles involving a divalent cation, which is also responsible for the sluggish cathodic kinetics and early capacity fade [5,12–14]. In addition, the electrochemical mechanism is rather complex and encompasses multiple steps that may result in irreversible phase changes [1]. Amongst the proposed materials, manganese oxides [15–21], vanadium oxides [21,22], vanadium phosphates [1,23], metal vanadates [1,23], Prussian blue analogues (PBAs) [24], and some organic redox-active compounds [25,26] have been considered. Manganese oxides are particularly interesting, thanks to the abundant and low-toxicity nature of Mn, which is available in various oxidation states (from +2 to +7) leading to several oxide phases and structures [1]. In previous works, MnO [27,28], Mn_3O_4 [29–32], Mn_2O_3 [33–35], amorphous MnO_x [36,37], and MnO_2 polymorphs (α [38,39], β [18,40], γ [16,19], δ [41,42], ε [43], λ [44], and todorokite [45]) were tested as potential cathode materials for AZIBs. Another alternative is zinc manganite, indicated by the general formula $Zn_xMn_{3-x}O_4$ [46–48], whose main representative is $ZnMn_2O_4$ (ZMO), also known as hetaerolite. Zinc manganites are a family of normal spinel oxides in which the cooperative Jahn-Teller distorted Mn^{3+} cations lead to a tetragonal distortion of the overall crystal (which belongs to the $I4_1/amd$ space group) [47–49]. The ideal spinel framework of ZMO, bearing a theoretical specific capacity of 224 mAh g^{-1} [50], is reported to be unsuitable for the reversible insertion/extraction of Zn ions [51,52]; however, proper nanostructuring, doping, introduction of stoichiometric defects, compositing with other materials, and exploitation of reaction mechanisms different from mere Zn^{2+} insertion/extraction may make this material an interesting candidate for AZIBs [53]. For example, Zhang et al. fabricated non-stoichiometric $ZnMn_2O_4$, in which the presence of abundant Mn vacancies promoted the Zn^{2+} insertion, thanks to a lower electrostatic repulsion between the host cations and the divalent charge carriers [51]. In a similar approach, Zhang et al. introduced oxygen defects to tailor the electronic conductivity, the ion diffusion kinetics, and the energy barrier for ion mobility [54], while Lee et al. prepared Zn-rich manganite microspheres, with nominal stoichiometry $Zn_{1.67}Mn_{1.33}O_4$ [55]. Interestingly, Wu et al. used a low-temperature synthesis to prevent the structural water from being removed from the lattice, which had a beneficial effect on the Zn^{2+} insertion and interfacial resistance [56]. Nanostructuring and compositing with various types of conductive carbon nanostructures are other effective approaches to improve the electrochemical performances and the structural stability of ZMO [57–65], as well as elemental doping. For example, Baby et al. reported the improved performances of Co-substituted ZMO ($ZnMnCoO_4$, ZMCO) [50], Tao et al. highlighted the positive effect of Ni and Co co-substitution to suppress the Jahn-Teller distortion [66], Cai et al. investigated the impact of Al^{3+} substitution in Zn^{2+} sites [67], and Shao et al. controlled the formation of oxygen defects in the ZMO lattice by double-doping with K and Fe [68]. Finally, synergistic electrochemical effects could be achieved by compositing ZMO with Mn_2O_3 [69–71] or Ti-MXenes [72]. In general, ZMO can be regarded as the Zn-analogue of $LiMn_2O_4$ and suffers from the same drawbacks as manganese oxides cathodes, *i.e.*, poor electronic conductivity, structural instability, poor rate performance, irreversible phase transformations, and Mn dissolution during cycles [1,5,64]. In addition, the electrochemical mechanism of ZMO-based materials in the presence of a Zn^{2+}- and Mn^{2+}-containing electrolyte is still unclear, and several mechanisms have been reported to occur and/or to coexist, such as: Zn^{2+} insertion/extraction [51,64], H^+ insertion/extraction [54,62], Zn^{2+}/H^+ co-insertion accompanied by the formation of zinc hydroxide sulphate hydrate (ZHS) [56,65,73,74], and reversible deposition/dissolution of MnO_x from the electrolyte [75].

Herein, we report on the synthesis of ZMO thin films by Pulsed Laser Deposition (PLD), a technique that, to the best of our knowledge, has never been employed to grow ZMO-based materials. A thin film can be used as a model system to study the electrochemical behaviour of the pure material; indeed, a film offers unique advantages for materials-science investigations, including: improved diffusion kinetics for ions and electrons, possibility to investigate novel materials and structures, and self-supported nature, deriving from the absence of polymeric binders and conductive additives [76]. In addition, beyond fundamental studies, thin films electrodes can be directly implemented in real-life thin-film microbatteries [77,78]. PLD is a highly versatile physical technique that allows the deposition of practically any material and the growth of nanostructured thin films whose properties can be easily tuned in terms of morphology, porosity, stoichiometry, structure, crystallinity, and phase by controlling a few deposition parameters [79,80]. In this work, ZMO thin films fabricated by PLD are fully characterized in terms of compositional, structural, and optical properties, and then employed in half-cells to assess their electrochemical behaviour and material modifications. Based on the approach previously developed in [81], electrochemical measurements on ZMO thin films in aqueous electrolyte are complemented by SEM and Raman studies.

2. Experimental

2.1. Synthesis of thin films

ZMO thin films were synthesized by PLD in a stainless-steel vacuum chamber, equipped with a primary scroll pump and a turbomolecular pump, connected in series, able to evacuate the chamber down to a base pressure of 1–4 × 10^{-3} Pa. Ablation was performed at room temperature using a frequency-doubled Nd:YAG laser source, in particular the 532 nm second harmonic, with 5–7 ns laser pulses and a repetition rate of 10 Hz. The laser pulses struck the target at an incidence angle of 45° and with an elliptical spot whose size was fixed at ~6 mm^2 by properly focusing the laser pulses. The resulting laser fluence on the target was varied in the range 2–6 J cm^{-2} by adjusting the pulse energy. The target was a Mn_2O_3:ZnO (1:1 mol%) vacuum hot-pressed pellet (99.99%, Testbourne B.V.), mounted on a support able to rotate and translate during deposition to ensure a uniform ablation. The chamber was also equipped with a quartz crystal microbalance (QCM) to estimate the deposited mass and consequently the film density. Depositions were carried out both in vacuum and in O_2 gas (Sapio, 5.0 purity), whose pressure was tuned by mass flow controllers at 1, 10, 30, 50, 70, 100, and 150 Pa. The substrate was placed on a rotating holder at constant distance from the target of 5 cm. Silicon ⟨100⟩ (Siegert Wafer), soda-lime glass slides (Marienfeld), and F-doped SnO_2 (FTO)-coated soda-lime glass slides (Sigma-Aldrich) were used as the substrates. Glass-based substrates were cleaned with isopropyl alcohol in ultrasonic bath before the insertion into the PLD chamber and dried with compressed air. The deposition time was selected according to the deposition rate and depending on the expected film thickness. Some samples were annealed in air using a Lenton Muffle furnace (ECF type) at different temperatures (400–800 °C).

2.2. Characterization

A field emission scanning electron microscope (FE-SEM, Zeiss SUPRA 40) was used to acquire top view and cross-sectional morphological images of thin films deposited on Si and FTO-coated glass. The film composition was evaluated by energy-dispersive X-ray spectroscopy (EDXS) using a Peltier-cooled silicon drift detector (SDD) within the SEM microscope (Oxford Instruments) and elaborated using the AZtec EDS software. Raman spectroscopy was used to gain information about the structure and the crystallinity of the films. A Renishaw InVia micro-Raman spectrometer equipped with a diode-pumped solid-state laser emitting 532 nm excitation radiation was used. The laser was focused on the sample using a 50× objective and the laser power was selected so as to avoid any photo-induced damage to the sample (typical values were 0.7–1.75 mW). For the quasi-*in situ* Raman characterization after the

electrochemical measurements, a Confotec NR500 spectrometer by Sol instruments was used, equipped with a solid-state laser (λ=532 nm, laser power on sample ~0.6 mW) and a 40× objective. X-ray diffraction (XRD) was employed to investigate the crystalline structure of the films. A HRD3000 diffractometer (Ital Structures, Riva del Garda, Italy) operating with monochromated Cu Kα radiation (λ=0.1541 nm) and equipped with a curved position-sensitive multichannel gas-filled detector (2θ range 0–120°, resolution 0.029°, Inel CPS-120) was used. The XRD measurements were carried out in grazing incidence configuration (GIXRD) with an incidence angle of ω=2°. The optical properties of films deposited on soda-lime and FTO-coated glass were probed by direct transmittance in the range 190–1100 nm using a Shimadzu UV-1800 spectrophotometer, and by transmittance and reflectance in the range 250–2000 nm using a PerkinElmer Lambda 1050 spectrophotometer equipped with a 150 mm-integrating sphere.

2.3. Electrochemical characterization

The electrochemical behaviour of as-deposited and annealed ZMO films on conductive FTO-coated glass slides was investigated in a three-electrode configuration and using a home-made electrochemical cell. Briefly, the sample was placed on top of a stainless-steel support and electrically insulated by a polymeric gel. Electrical contacts were made by attaching a Cu wire to the exposed FTO layer with Cu tape. A PTFE case equipped with a VITON O-ring was directly pressed on the sample and fixed by screws to the support, then it was filled with the liquid electrolyte (total volume ~1 mL). The area of the film exposed to the electrolyte was ~0.4 cm^2. Two platinum wires were inserted into the cell, one turning around the whole cell and operating as the counter electrode, and one acting as a quasi-reference (Pt-QRef) electrode. The potential shift of the Pt-QRef electrode with respect to the Ag/AgCl (KCl 3.5 M) reference electrode was experimentally determined in a two-electrode cell to be +0.445 V, with stability within a few mV in the investigated electrolytes. All potentials reported have been referenced to the Ag/AgCl scale. ZMO samples were tested in aqueous electrolytes containing 2 M $ZnSO_4$ (ZS), 0.1 M $MnSO_4$ (MS), or 2 M $ZnSO_4$ + 0.1 M $MnSO_4$ (ZMS), prepared in deionized water from zinc sulphate heptahydrate ($ZnSO_4 \cdot 7H_2O$, ≥ 99.0%) and manganese sulphate monohydrate ($MnSO_4 \cdot H_2O$, ≥ 98%), both purchased from Sigma-Aldrich. Cyclic voltammetry (CV) and other electrochemical measurements were performed using a PalmSens4 potentiostat/galvanostat/impedance analyser.

3. Results and discussion

3.1. Optimization of PLD parameters

PLD allows one to easily adjust the deposition parameters, especially the chamber pressure, the type of gas, the laser fluence, and the target-substrate distance, in order to fabricate a thin film with tuneable and optimizable properties and performances. ZMO thin films were grown in vacuum and at different O_2 pressures (1–150 Pa); the gas atmosphere affects the dynamics of plasma formation, cluster nucleation, and deposition [80], thus it mainly affects the resulting film morphology. SEM cross-sectional images of as-deposited ZMO films on Si as a function of the O_2 deposition pressure (laser fluence ~3.7 J cm^{-2}, deposition time = 15 min) are reported in Fig. 1a. Increasing the O_2 pressure from vacuum to 150 Pa, the film morphology changes from a compact columnar structure to a highly porous tree-like structure, along with a progressive increase of film porosity and surface roughness. At high oxygen pressures (100 and 150 Pa), the dense columnar structure is replaced by porous nanotrees. The increase of film porosity is accompanied by a sharp decrease in density (below ~1 g cm^{-3} for samples deposited at or above 50 Pa, as estimated from QCM measurements coupled with SEM images; for comparison, the density of bulk crystalline ZMO is 5.254 g cm^{-3} [82]) and by a corresponding increase in surface area and film thickness at fixed deposition time. The morphology evolution as a function of the background gas pressure described above is typical of PLD-grown oxides and nitrides thin films [80,83–87]. The laser fluence (*i.e.*, the laser energy per unit area striking the target) has a less evident effect on film morphology. In addition to an expected increase of the deposition rate at constant O_2 pressure, higher fluences lead to more compact films and, especially at high O_2 pressures (≥ 50 Pa), cause the detachment of the growing film from the substrate, the film breakup, and the presence of a larger number of defects (Fig. S1). As a result, a reasonable fluence of ~3.7 J cm^{-2}, corresponding to energies of ~225 mJ $pulse^{-1}$, was selected for subsequent depositions as a compromise between deposition rate and film quality. Typical deposition rates at this fluence range from some tens of nm min^{-1} in vacuum/low O_2 pressure up to hundreds of nm min^{-1} above 50 Pa. O_2

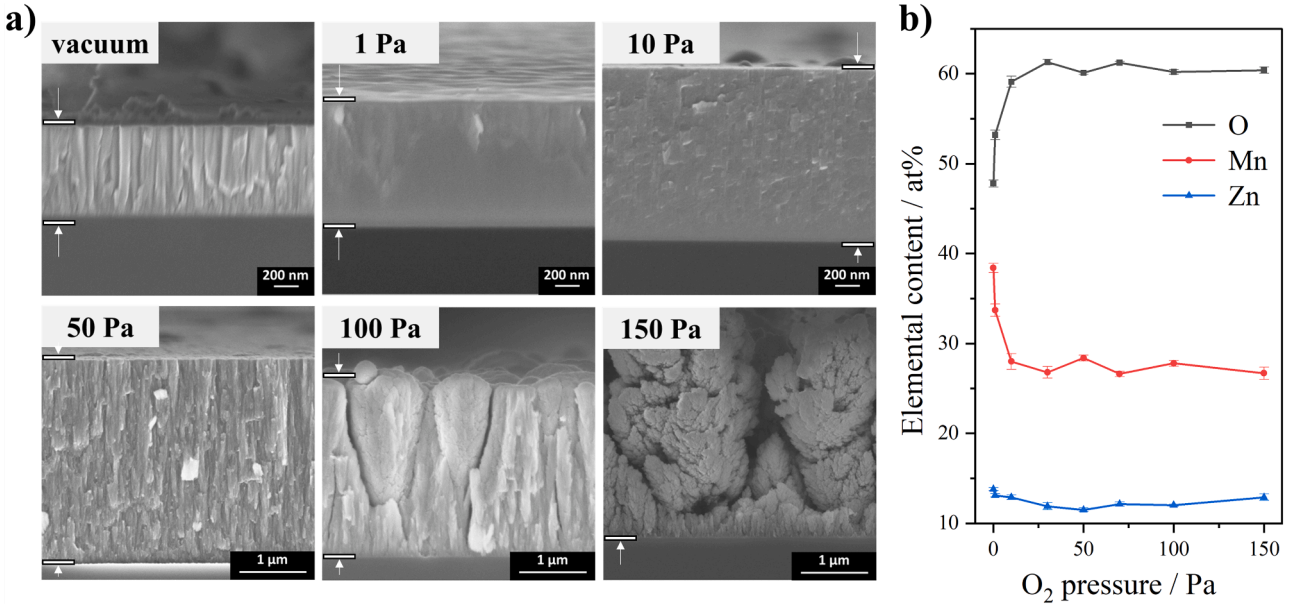

Fig. 1. (a) SEM cross-sectional images of the ZMO thin films deposited on Si at different O_2 pressure, at constant laser fluence of ~3.7 J cm^{-2} and 15 min deposition time. (b) EDX elemental analysis of as-deposited ZMO films.

background atmosphere also affects the film stoichiometry, which can be modified with respect to the nominal composition of the target by depositing in a reactive gas. As depicted in Fig. 1b, where EDX elemental analysis is reported, our as-deposited films are enriched with oxygen as the O_2 deposition pressure increases up to ~30 Pa, with the O atomic content in the films rising from 48% (vacuum) to >60% (30 Pa). This increase is accompanied by a decrease in the Mn atomic content (from 38% to 27%), while the Zn atomic content shows much less variability (between 11% and 14%) in the whole O_2 pressure range.

Structural information about ZMO films was gained by Raman spectroscopy. Raman spectra of all as-deposited films at any O_2 pressure and laser fluence show a weak and broad band centred around 600 cm^{-1} and extending in the range 450–750 cm^{-1}, indicating an amorphous nature of the film (Fig. 2a, black spectrum).

3.2. Thin films annealing

In order to promote the film crystallization, as-deposited ZMO films were subjected to thermal treatments in air in the temperature range 400–800 °C. Film crystallization to the expected spinel phase [46,49,88,89] was achieved at any temperature above 450 °C, as confirmed by the Raman spectrum of the annealed film of Fig. 2a, where sharp peaks are observed. Three main peaks are found at 325, 385, and 679 cm^{-1} (the latter mode can be assigned to A_{1g} symmetry [49]), while additional shoulders and weak features are observed also at 302, 373, 475, 587, and 652 cm^{-1} (Fig. S2), all well matching with the reported Raman bands of $ZnMn_2O_4$ [46,49]. No signals from secondary phases were detected. In Fig. 2b, the EDX elemental analysis of ZMO films deposited at different O_2 pressures and annealed in air at 600 °C for 3 h are reported. Although EDX suffers from low accuracy in the quantification of light elements, which entails uncertainties in the absolute values especially in the absence of calibration samples, the overall trends of the atomic contents with respect to O_2 pressure are still relevant. After the thermal treatment, the atomic content of Zn and Mn increases compared to as-deposited films, while the O atomic content decreases (at least for samples deposited at ≥10 Pa O_2). None of the elements, however, matches the atomic percentages of stoichiometric $ZnMn_2O_4$, indicated by grey dashed lines in Fig. 2b. All the films contain a lower amount of oxygen (52–55%) with respect to the theoretical value of ~57%, and a higher amount of Mn, which may indicate the presence of Mn ions with a lower oxidation state (*i.e.*, Mn^{2+}), and the possible localized formation of spinel hausmannite Mn_3O_4, isostructural to $ZnMn_2O_4$ [49,90,91].

SEM images of ZMO films after annealing are reported in Fig. 3a (cross-sections) and in Fig. S3 (top-views). The morphology is completely different from that of as-deposited films (Fig. 1a). Films are polycrystalline, with morphological grains ranging from hundreds of nm to ~50 nm as the O_2 deposition pressure increases. In addition, the columnar and compact structure of films deposited in vacuum and 10 Pa is replaced by large faceted crystalline grains and by some voids and cavities (Figs. 3a and S3), qualitatively indicating a higher degree of porosity compared to as-deposited films, also for low O_2 deposition pressures. For films deposited at 50 and 100 Pa, small crystalline grains (50–100 nm) assemble into vertical structures resembling the original nanotrees. The Raman spectra of annealed films deposited in vacuum and at 1, 10, 50, and 100 Pa of O_2 are reported in Fig. 3b and were analysed using Lorentzian fittings. The three main Raman bands of spinel ZMO (here labelled as peak I, II, and III, respectively) exhibit a blueshift as the deposition pressure increases (Figs. 3c and S4a-b), which is more relevant for the high-frequency A_{1g} mode (peak III) [49]. Indeed, peak III shifts from 673.8 cm^{-1} to 680.3 cm^{-1} as the O_2 deposition pressure is increased from vacuum to 150 Pa. In addition, the intensity ratio between peak I and peak III is reversed with increasing O_2 pressure: indeed, the A_{1g} peak (peak III) is the most intense in the Raman spectra of crystalline samples deposited in vacuum and at 1 Pa, whereas peak I becomes dominant at or above 10 Pa (Fig. 3c). Such variations in peak position and relative intensity may be ascribed to the effect of crystallite size only [92], however similar trends are reported also by Nádherný et al. [46] and correlated to the amount of Zn in the manganite structure, *i.e.*, to the stoichiometric x value in $Zn_xMn_{3-x}O_4$. Since the atomic contents of Mn and Zn in the films after crystallization are not constant (Fig. 2b) and no secondary phases are detected by Raman spectroscopy and SEM imaging, the modifications observed in the Raman spectra of Fig. 3b might be attributed to slight changes in the relative contents of metallic elements in the overall manganite structure. The differences

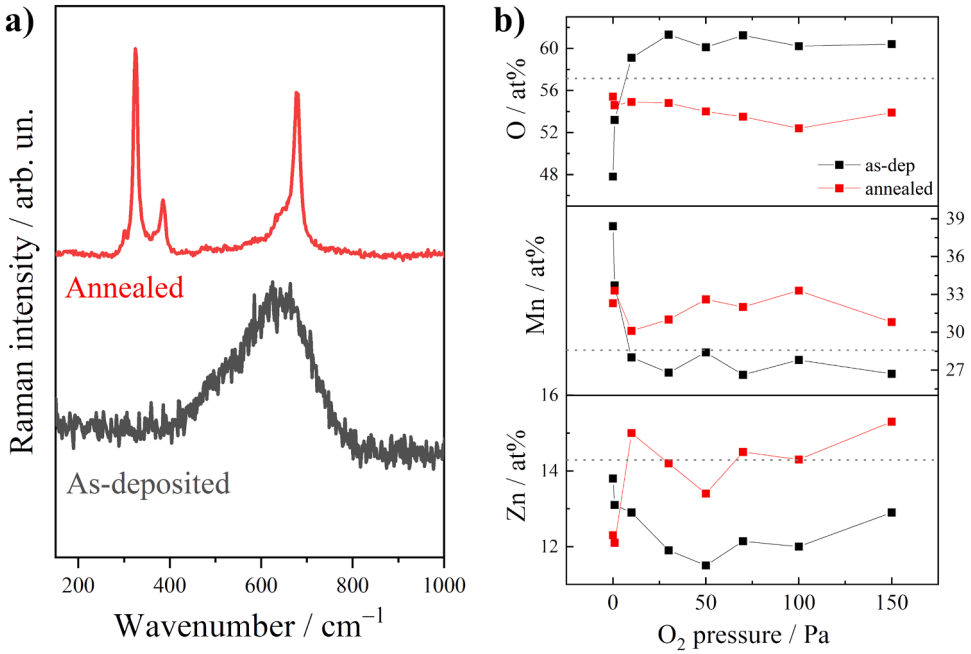

Fig. 2. (a) Comparison between the Raman spectra of the ZMO film deposited at 50 Pa of O_2 (~3.7 J cm^{-2}) before and after air annealing at 600 °C, 3 h. (b) EDX elemental analysis of air-annealed ZMO films (600 °C, 3 h); for comparison, also the atomic content of as-deposited samples is reported. The grey dashed lines correspond to O, Mn, and Zn atomic percentages in ideally stoichiometric $ZnMn_2O_4$.

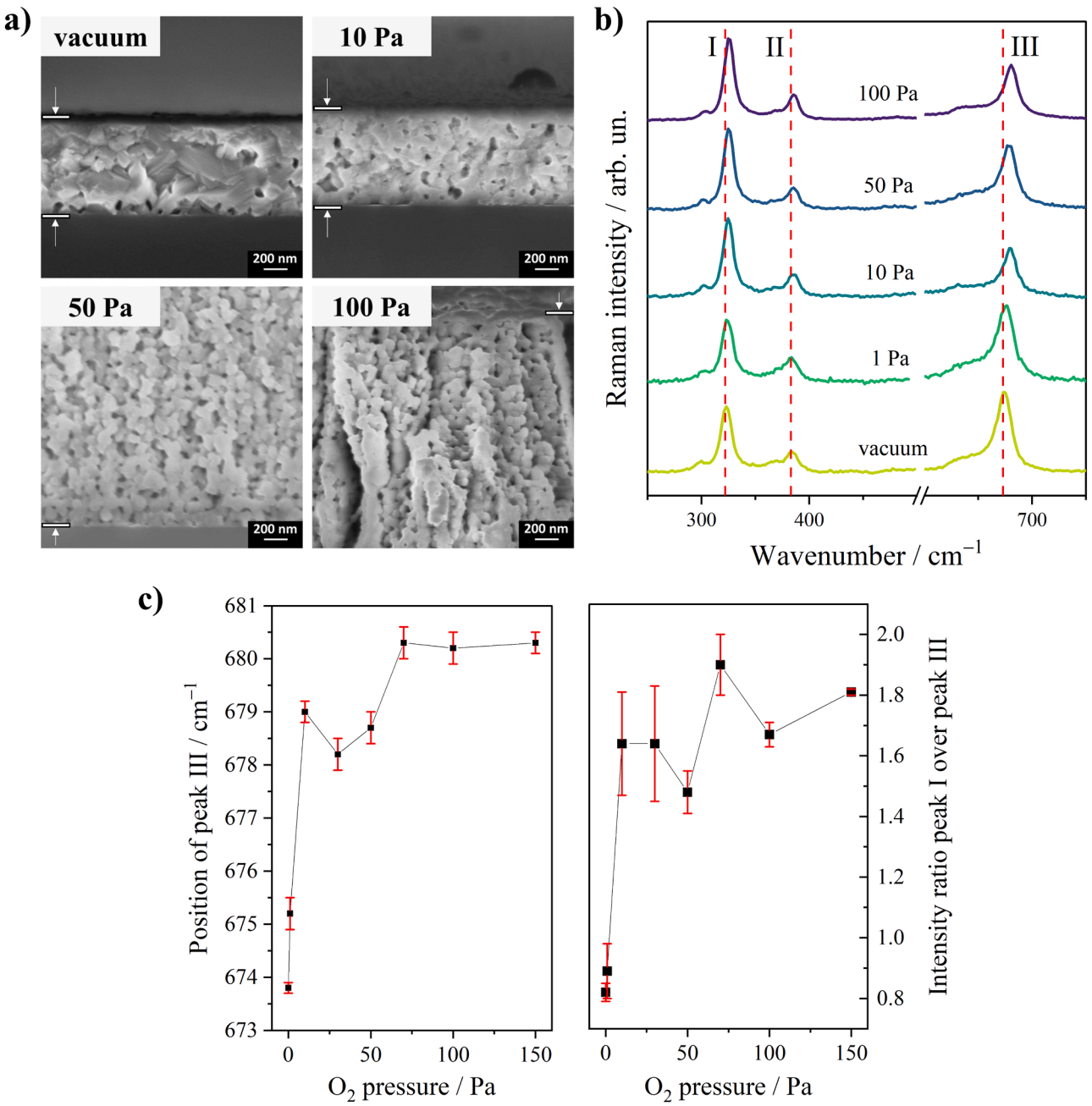

Fig. 3. (a) SEM cross-sectional images of the ZMO thin films air-annealed at 600 °C, 3 h, and deposited on Si with constant laser fluence of ~3.7 J cm^{-2} and in vacuum, 10 Pa, 50 Pa, and 100 Pa of O_2. (b) Evolution of the Raman spectral features of crystallized samples as a function of the O_2 deposition pressure (the three main peaks are here labelled as I, II, and III). (c) Position of peak III (A_{1g} mode) and intensity ratio between peak I and peak III as a function of the O_2 deposition pressure.

observed in peak position and relative intensity ratios with increasing O_2 deposition pressure are not associated with a clear trend in peak width (Fig. S4c). Compared to the Raman spectra of spinel Mn_3O_4 reported in [92], which correlates the progressive redshift and broadening of the main A_{1g} peak with decreasing crystallite size from >100 nm to 7 nm, our spectra exhibit a general blueshift and no specific peak broadening or narrowing as the O_2 pressure increases. This may indicate that the crystal size does not play the major role in affecting the Raman spectra of annealed ZMO thin films. In addition, annealing in air of selected samples at different temperatures (500, 600, 700, and 800 °C) demonstrated that the Raman spectra are not affected by the increase in temperature, even if the ZMO crystalline grains get bigger as the annealing temperature increases (Figs. S5 and S6a). In this case, a gradual decrease of peaks width confirms the improvement of crystalline quality with increasing annealing temperature (Fig. S6b). Film crystallization is further confirmed by GIXRD measurements. The X-ray diffraction patterns of ZMO films produced in vacuum and at 1, 10, 50, and 100 Pa of O_2 are reported in Fig. 4, along with the powder reference pattern of tetragonal spinel hetaerolite $ZnMn_2O_4$ (Card No: 6990, WWW-MINCRYST [93,94]). Good agreement with the reference pattern is observed for ZMO films produced at 50 and 100 Pa, which exhibit the most intense (211) reflection at 2θ~36.40° and consistent intensity ratios. The X-ray data at 10 Pa are coherent as well, even though the (103) reflection is absent and some discrepancies affect the relative intensity ratios, especially the (112) *vs.* (200) and the (321) *vs.* (224). In contrast, the main reflection in the GIXRD pattern of the ZMO film produced at 1

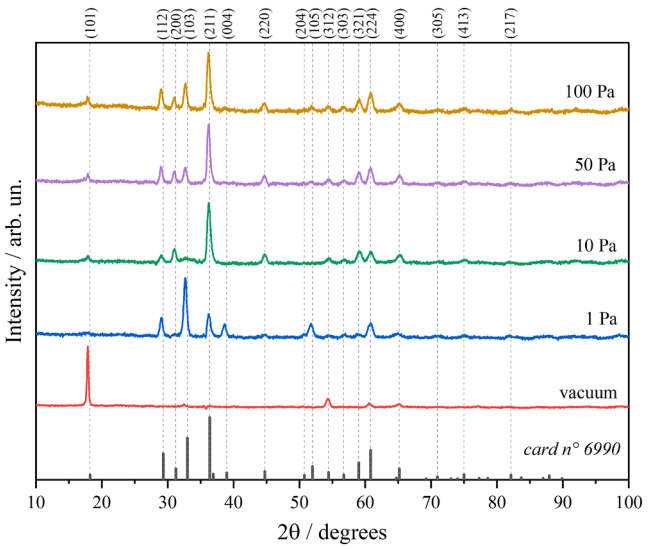

Fig. 4. GIXRD patterns of crystalline ZMO thin films, produced at different O_2 pressures and annealed in air at 600 °C, 3 h.

Pa is the (103) at 2θ~32.67°, and the (200), (220) and (400) reflections are weak or totally suppressed. Finally, the X-ray diffraction pattern of the ZMO sample produced in vacuum exhibits one sharp and narrow peak at 2θ~17.87°, corresponding to the (101) reflection, while most of other reflections are suppressed, except for the (312), (224), and (400). The XRD results reveal a different preferential crystalline orientation within ZMO films produced in vacuum and at 1 Pa O_2 and suggest that the O_2 deposition pressure affects not only the short-range order of the material (as confirmed by the modifications in the Raman spectra, Fig. 3b-c), but also the long-range crystalline texture.

Quantitative analysis was carried out using the Williamson-Hall (WH) method [95,96], which allows the estimation of the average size of crystal domains and of the lattice micro-strain through the broadening of the XRD peaks (Fig. S7a-e). As expected, the domain size is maximum in the ZMO film produced in vacuum (τ~63 nm) and it decreases down to τ~57 nm and τ~27 nm for films deposited at 1 and 10 Pa, respectively; it remains almost constant in the film produced at 50 Pa (τ~29 nm), but it raises to τ~38 nm at 100 Pa (Fig. S7f). The lattice micro-strain is found to be positive in all the films, *i.e.*, indicating the presence of a tensile stress state, and it is maximum in the film deposited at 1 Pa (Fig. S7f). Raman spectroscopy and GIXRD results clearly indicate that the O_2 deposition pressure is a key parameter affecting the structural ordering of the ZMO thin films at both the short/medium range and the long range. In particular, GIXRD measurements highlighted the evolution of the preferential crystal orientation, the variation of the crystal size, and the occurrence of lattice micro-strains, while the modifications of the Raman spectra may be correlated to the Zn stoichiometry according to [46]. However, additional effects may contribute to the overall shift and broadening of the ZMO Raman peaks, *e.g.*, the residual stress state, the presence of traces of secondary phases, the oxygen deficiency, and the crystal size, therefore the trends observed in Figs. 3b-c and S4 may result from multiple and interrelated causes.

3.3. Optical properties of annealed films

ZMO thin films were deposited on glass and FTO-coated glass slides, with the purpose of carrying out optical measurements. The deposition time, at any value of O_2 pressure and constant fluence of 3.7 J cm^{-2}, was adjusted to achieve a film thickness in the range 500–600 nm, depending on the deposition rate previously evaluated on samples deposited on Si in similar conditions. Before annealing, ZMO thin films exhibit a dark reddish colour, which turns orange/yellow after thermal treatment in air (Fig. S8a). Since the thermal stability of the glass support is limited to ~550 °C, annealing of ZMO films on bare glass and FTO-coated glass was performed at 500 °C for 2 h. This temperature allows good film crystallization, as evaluated by Raman spectroscopy and SEM analysis (Fig. S8b-c). In Fig. 5, UV–Vis transmittance, reflectance, and absorption curves in the wavelength range 300–2000 nm for ZMO samples deposited on soda-lime glass at 1, 10, 50, and 100 Pa of O_2, and crystallized in air at 500 °C for 2 h, are reported. Transmittance and reflectance data of Fig. 5a-b were collected in a spectrophotometer equipped with the integrating sphere and account for both direct and diffuse contributions. Absorption data are estimated by the relation:

$$A(\lambda,\%) \cong 100 - T(\lambda,\%) - R(\lambda,\%)$$

Transmittance and absorption curves (Fig. 5a and c) exhibit a small blueshift as the deposition pressure increases. In addition, the number of interference fringes in the transmittance curves decreases with increasing O_2 pressure as well. Similarly, the increase of surface roughness leads to less defined fringes as the O_2 pressure increases. Absorption curves of Fig. 5c feature extended sub-bandgap optical absorption in the range 600–750 nm, which may indicate the presence of defect states in the mid-gap region of the material [89]. In Fig. 5d, absorption curves are reported as a function of photon energy, in the range 0.5–4.5 eV, for comparison.

Similar results are obtained by measuring the direct transmittance of ZMO films deposited on FTO-coated glass at the same deposition conditions in terms of laser fluence and O_2 pressure as on the bare glass slides (Fig. S9), with average thickness ~500–600 nm. The slight blueshift of the transmittance curves observed in Fig. 5a as the O_2 pressure increases is still present, even if some deviations are observed, *e.g.*, for the film deposited at 50 Pa. Such variations may be ascribed to the effect of the substrate on film morphology or, more likely, to the contribution of the diffuse transmittance, which is lost during measurements of direct transmittance and could be relevant for porous samples.

3.4. Electrochemical properties of annealed films

The schematic illustration for the preparation of crystalline ZMO thin films on an FTO-coated glass substrate for electrochemical characterization is reported in Fig. 6. All the films were grown by PLD in O_2 atmosphere with tuneable morphology and average thickness in the range 500–600 nm, and then they were thermally annealed in air at 500 °C for 2 h to achieve the proper spinel phase without damaging the glass substrate.

The CV profiles of the ZMO thin film grown at 50 Pa of O_2 are reported in Fig. 7. CV was performed in ZMS electrolyte at a scan rate of 1 mV s^{-1}. We have selected this electrolyte because it is the standard for AZIB studies: it is worth noting that differences in composition amongst MS, ZS, and ZMS electrolytes have a specific impact on the structural evolution upon cycling of MnO_x-based electrodes [81]. CV cycling was carried out in a potential range spanning Mn reactivity between reduction to Mn^{2+} and oxidation to Mn^{4+}. The complex voltammetric patterns, corresponding to combined Mn-redox and phase-transformation/film-formation, can be interpreted in the methodological framework set in [81]. Cycling was started from 0.55 V with an anodic-going scan, that exhibits a weak anodic peak at ~0.8 V and a current onset at ~0.9 V. These processes, in principle, can correspond to phase formation by oxidation of Mn^{2+} present in the electrolyte and oxidation of Mn^{3+} present in ZMO, converting to a Mn^{4+}-containing phase. The first cycle is markedly different from the following ones, indicating an activation/transformation process of the film, which is frequently reported for Mn- and ZMO-based electrode materials [59,63]. In the anodic branch, starting from the second cycle, the two features observed in the first anodic-going scan are notably activated by the reduction processes observed in the cathodic-going scan – discussed below – and develop into a couple of oxidation peaks. These peaks are initially centred at 0.75 V and 0.86 V and exhibit a progressive shape

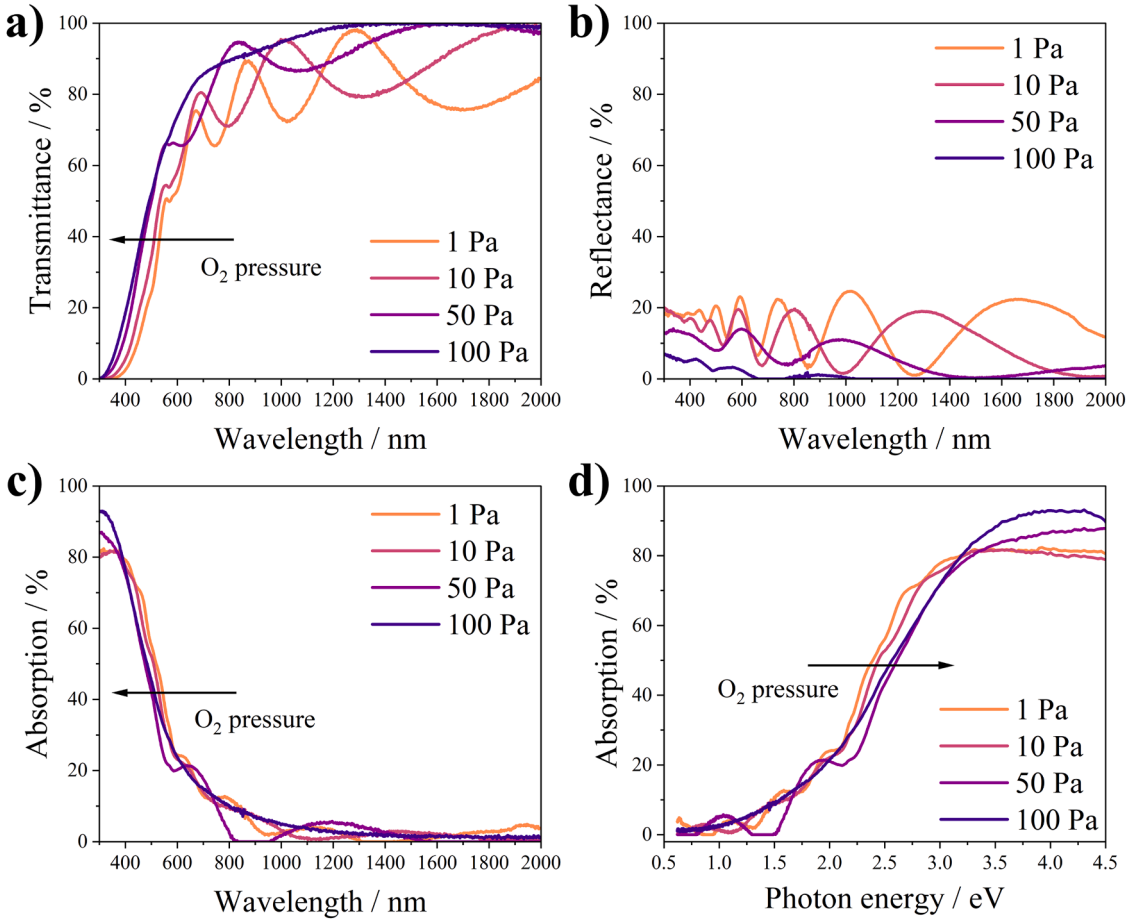

Fig. 5. UV–Vis (a) transmittance, (b) reflectance, and (c) absorption curves in the wavelength range 300–2000 nm of crystalline ZMO samples deposited at 1, 10, 50, and 100 Pa of O_2, and annealed in air at 500 °C for 2 h. (d) UV–Vis absorption curves plotted as a function of photon energy in the range 0.5–4.5 eV.

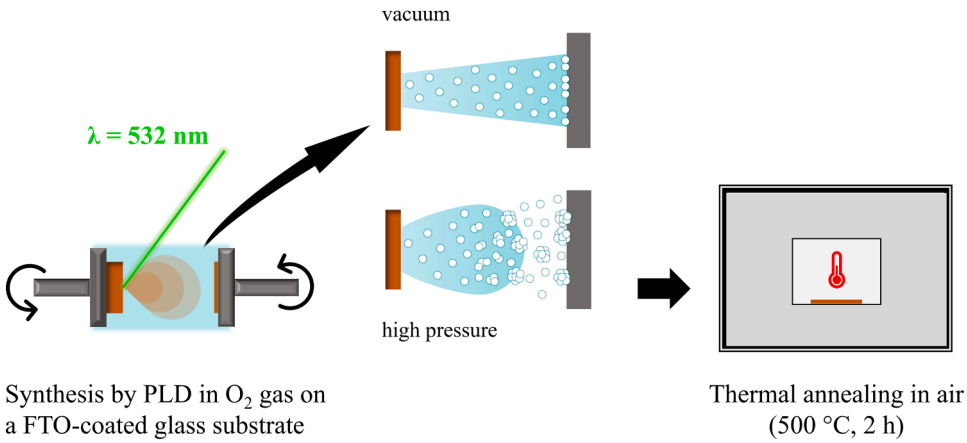

Fig. 6. Schematic illustration of the preparation of ZMO thin films for the purpose of the electrochemical characterization.

change and the tendency to shift towards higher potential values, as the number of cycles increases. These modifications of the anodic CV features can be ascribed to a progressive phase transformation, as detailed below. As far as the cathodic branch is concerned, a couple of reduction peaks can be observed, that exhibits a notable change between the first and the subsequent cycles. Similarly to the anodic counterpart, prolonged cycling leads to progressive peak shift in the anodic direction in the ranges 0.34–0.4 V and 0.49–0.55 V, respectively. Our CV curves agree with those reported in previous works and corresponding to various ZMO-based nanostructures in the same electrolyte solution [60,69,75]. The assignment of the redox peaks to a specific electrochemical process is not unique since multiple concurrent processes may occur at the electrode-electrolyte interface, yielding very similar current responses, and the scientific literature is not unanimous. During the anodic scan, the oxidation peaks could be ascribed to both the extraction of Zn^{2+} from the host lattice, accompanied by the stepwise oxidation of Mn^{3+} to Mn^{4+}, and to the electrodeposition of MnO_x interphases from Mn^{2+} species present in the electrolyte, either because of its formulation or originating from the cathodic dissolution of the film material. During the cathodic scan, these processes are reversed. Overall, cycling seems to

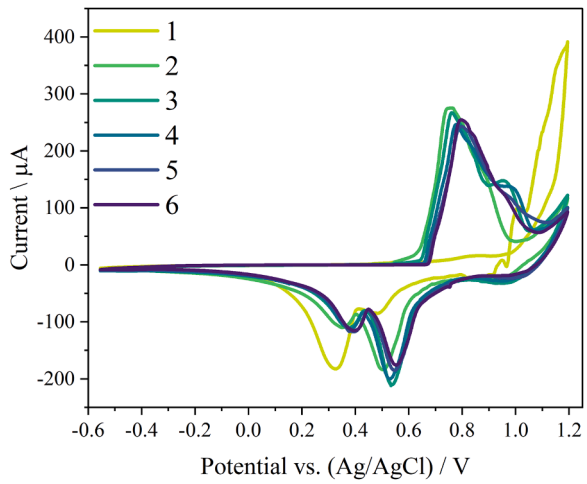

Fig. 7. CV curves at a scan rate of 1 mV s^{-1} of the ZMO thin film deposited at 50 Pa of O_2 and crystallized in air at 500 °C, 2 h.

lead to a stable voltammetric pattern, featuring a couple of reversible redox processes involving a solid electrode/electrolyte interface.

In order to gain better insight into the nature of these electrochemical material transformations, we resorted to *ex situ* structural and morphological characterization. After having completed the CV cycling experiments of Fig. 7, the aged ZMO sample was extracted from the cell, immediately rinsed in deionized water, and gently dried to remove any trace of soluble sulphates. In Fig. 8a, a SEM cross-sectional image of the aged film at the end of the sixth cycle is depicted, revealing a profound modification with respect to the morphology of the pristine film (not shown, but reasonably comparable with the cross-section of Fig. 3a). Specifically, a clear multi-layered structure develops from the initial columnar and granular morphology: starting from the bottom part of the image, the first layer resembles the structure of the original film, even if its thickness is reduced (to ~300 nm) and the morphology is slightly changed (Fig. 8b), denoting some degree of electrochemical activity. The second layer (thickness ~800–900 nm) consists of a porous, thick deposit, which can be identified by Raman spectroscopy (Fig. 8c) as MnO_x [97], originating either from the electrodeposition of Mn^{2+} in the electrolyte, or from the transformation of the ZMO film. Finally, the third layer is constituted by thin, water-insoluble flakes. This peculiar flake-like morphology (Figs. 8a and S10a) suggests the precipitation of zinc hydroxide sulphate hydrate (ZHS) $Zn_4(OH)_6(SO_4)•nH_2O$ phase, commonly reported in previous works as a by-product formed during the discharge of AZIBs in near-neutral aqueous electrolytes containing Zn sulphate [60,62,75,98]. The formation of ZHS is conventionally associated with proton insertion into the active film during the cathodic scan, leading to an increase of the pH of the electrolyte surrounding the film, and to the precipitation of this basic compound that acts as a buffer [98]. The presence of ZHS is confirmed by both Raman spectroscopy, *i.e.*, the peaks at 969 and 1015 cm^{-1} [98] (Fig. 8c), and EDXS, which

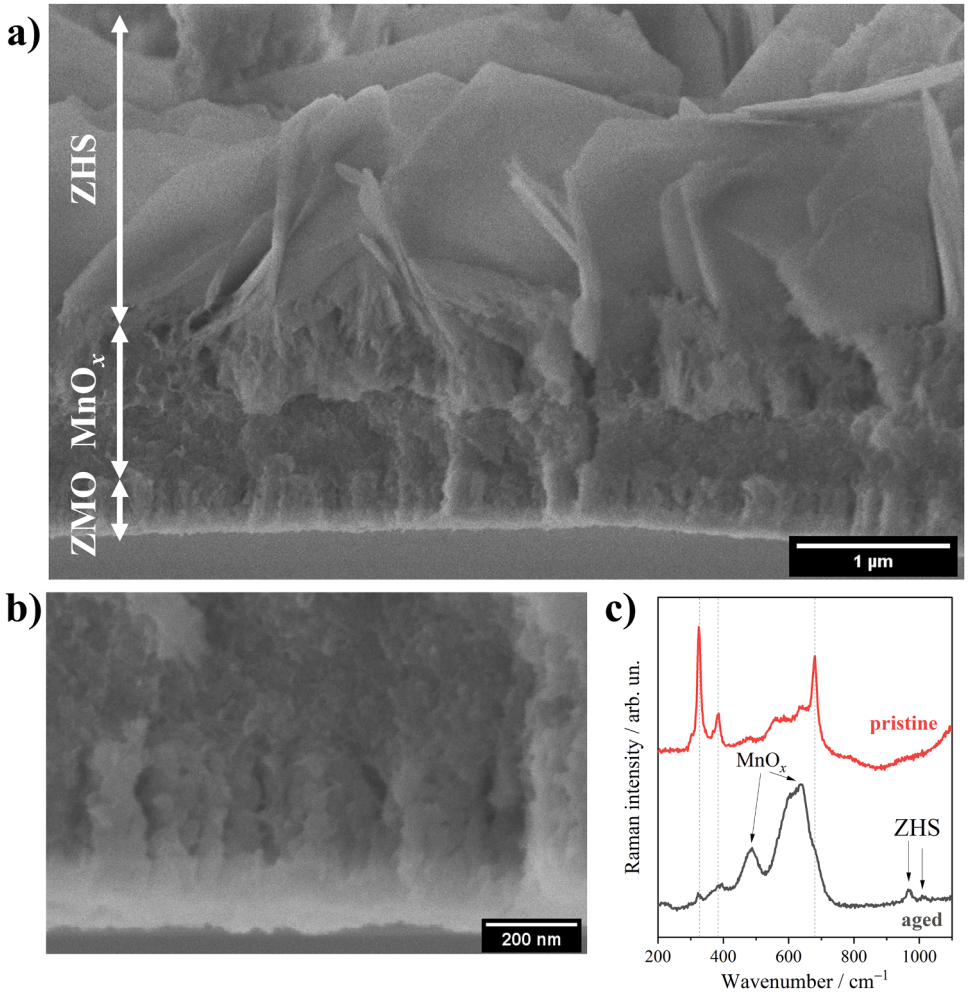

Fig. 8. SEM cross-sectional image of (a) the whole aged ZMO film and (b) the bottom layer after 6 CV cycles at 1 mV s^{-1}. (c) Raman spectra comparing the pristine (*i.e.*, after annealing) and the aged film. The characteristic Raman features of MnO_x and ZHS phase are highlighted.

reveals the occurrence of sulphur in addition to Zn, Mn, and O (Fig. S10b).

To highlight the effect of the film morphology on the electrochemical response of the material, additional CV measurements in ZMS electrolyte were carried out at a higher scan rate of 25 mV s^{-1} – de-emphasizing diffusion-controlled processes with respect to phase-formation ones – on ZMO films grown at 1, 50, and 100 Pa of O_2, corresponding to increasing porosity. The CV profiles are reported in Fig. 9, displaying the first eight cycles for each sample. It can be noticed that the shape of the CV curves differs significantly across the samples. Moreover, for a given sample, the CV responses at 1 and 25 mV s^{-1} are different (*e.g.*, compare Figs. 7 and 9b). Firstly, the redox peaks become more defined as the film porosity increases, *i.e.*, moving from 1 to 100 Pa. This is an indication of a diffusion-based process, which is facilitated both at lower scan rate and in samples exhibiting shorter diffusion paths. Secondly, all the curves show a progressive separation of the peaks towards higher potentials (in absolute value) as the cycles proceed. This effect, that was less evident at 1 mV s^{-1}, owing to the lower currents involved, is due to the formation of a resistive layer during the electrochemical cycling, leading to increased polarization. This phenomenon is progressively less evident as the porosity increases, especially in the case of the most porous film (Fig. 9c), the electrochemical response of which features sharper redox peaks and stabler cycle shapes compared to those of the less porous ones (Fig. 9a-b).

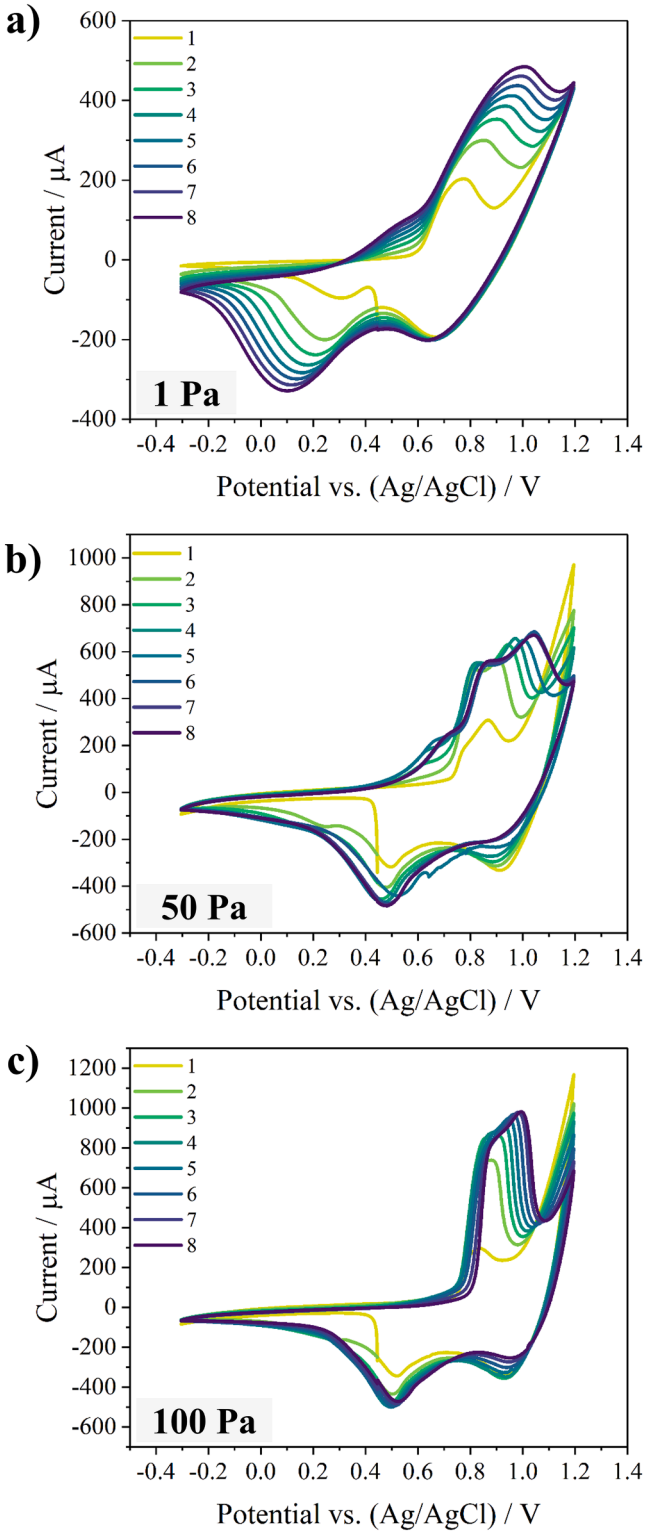

Fig. 9. CV curves at a scan rate of 25 mV s^{-1} of the ZMO films deposited at (a) 1, (b) 50, and (c) 100 Pa of O_2, and crystallized in air at 500 °C, 2 h.

After the CV test, the sample grown at 100 Pa of O_2 – which showed sharper and stabler redox peaks in the CV of Fig. 9c – was subjected to a series of constant potential measurements in ZMS electrolyte to promote the redox reactions and to evaluate the current response over time. At the same time, quasi-*in situ* Raman measurements were carried out to probe the sample structural evolution. The Raman results and the current *vs.* time profiles at selected potential values are summarized in Fig. 10 and Fig. S11, respectively. After the CV (curve b) the main ZMO features are still visible, however a broad band arises next to the A_{1g} peak and extends between 550 and 650 cm^{-1}. In addition, a broad peak starts to be visible at ~490 cm^{-1}. Both features indicate the formation of MnO_x during the CV cycles [64,97]. Cathodic polarization at 0.45 V for 1100 s partially restores the film to its initial conditions (curve c), reducing the intensity of the MnO_x bands: this behaviour is compatible with the incomplete dissolution of the MnO_x layer, which can also be accompanied by Zn^{2+} insertion into the MnO_x formed during the anodic branches of the CV run either from ZMO de-insertion or from oxidative electrodeposition of Mn^{2+} present in solution. Correspondingly, the cathodic current asymptotically approaches zero after 1100s (Fig. S11a). The following anodic polarization at 1.05 V for 1800 s leads to a significant decrease in the intensity of ZMO Raman peaks, in conjunction with the uprise of the MnO_x band (curve d), which can be explained with both Zn^{2+} de-insertion from ZMO and electrodeposition from the electrolyte. Moreover, the resultant anodic current profile does not approach zero, but it tends asymptotically to a current value of ~260 µA

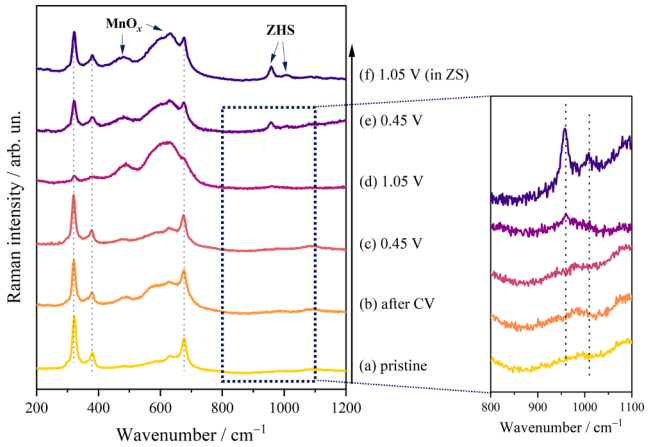

Fig. 10. Evolution of the quasi-*in situ* Raman spectra of a ZMO film (grown at 100 Pa of O_2 and annealed at 500 °C, 2 h) during sequential electrochemical measurements. In the inset, the spectral region between 800 and 1100 cm^{-1} is highlighted. Curves (a–e) were acquired after electrochemical polarization in ZMS electrolyte, while curve (f) was acquired after polarization in ZS electrolyte.

(Fig. S11b), suggesting an ongoing redox process. Finally, the Raman peaks of ZMO become clearly visible again after the second cathodic polarization at 0.45 V for 1500 s, even if the MnO_x features are still intense (curve e). The corresponding cathodic current profile approaches zero at the end of the measurement (Fig. S11c), indicating that the MnO_x phase cannot be totally and reversibly reduced at 0.45 V. In addition, as reported in the inset of Fig. 10, the peaks at 960 and 1008 cm^{-1} appear after the second cathodic polarization, revealing the precipitation of the ZHS phase [98]. Interestingly, ZHS was not present immediately after the CV at 25 mV s^{-1} (as it was in the case of CVs at 1 mV s^{-1}, see Fig. 8) since its formation evidently requires longer reaction times. The typical flake-like morphology of ZHS was also highlighted by SEM (Fig. S11e-g). Interestingly, in the absence of electroactive Mn^{2+} in the electrolyte – *i.e.*, using the ZS electrolyte – the Raman spectrum does not appreciably change upon anodic polarization at 1.05 V (compare curves e and f) and the current *vs.* time profile differs significantly from that observed when the same process is run in the ZMS electrolyte (compare Fig. S11b and S11d), exhibiting no asymptotic current value and a rapid decrease to zero (the measurement was stopped after 500 s). Notably, the high-frequency Raman peaks do not disappear, indicating no ZHS dissolution at this potential value. This last test in the ZS electrolyte confirms that the main redox process in the potential ranges investigated in this work involves the electrodeposition of MnO_x species from Mn^{2+} dissolved in the electrolyte, possibly accompanied by the reversible insertion/extraction of Zn^{2+} in these electrodeposited layers.

Lastly, in order to better distinguish between phase transformation and formation processes, CV measurements at 25 mV s^{-1} were performed also on bare FTO-coated glass substrates in the MS, ZS, and ZMS electrolytes, as reported in Fig. S12. No electrochemical activity is obviously reported in ZS electrolyte, due to the absence of redox-active species in the selected potential range. On the other hand, redox peaks are observed in both MS and ZMS electrolytes, which could be ascribed to the electrodeposition/dissolution of MnO_x on the surface from the Mn^{2+} in the electrolyte. The noticeable difference in CV shape and intensity denotes the role of Zn^{2+} in the electrochemical reactions, which may insert/de-insert into/from the electrodeposited MnO_x layer only in ZMS electrolyte. Our results are closely similar to those reported by Soundharrajan et al., which unravelled the dominant role of Mn^{2+} in the electrolyte on the electrochemical mechanism of $ZnMn_2O_4$-based materials [75], and to those of [81], which highlights the impact on the electrochemical response of MnO_x resulting from the presence of Zn^{2+} in the electrolyte.

4. Conclusions

In this work, we successfully synthesized ZMO thin films via PLD on different substrates. Using complementary characterization techniques, including SEM, EDXS, Raman spectroscopy, XRD, UV–Vis optical spectroscopy, we highlighted the effect of deposition (O_2 pressure, laser fluence) and annealing (temperature, duration) parameters on the variation of film morphology, composition, and crystallinity, which strongly affect the vibrational, structural, optical, and electrochemical properties of the material. The O_2 deposition pressure results to be the most significant synthesis parameter: by increasing the O_2 pressure from vacuum to 150 Pa, the ZMO film becomes more porous and less dense and, after crystallization upon thermal treatment in air, the effect of deposition pressure is still observable in the Raman features, the XRD crystal orientation, the stoichiometry, and the optical absorption of the film. Since bulk ZMO was previously reported to exhibit poor electrochemical activity in the presence of Zn^{2+} [51], a rationally designed ZMO material in terms of nano-porosity (and hence density and surface area), crystal size and orientation, phase purity, and Zn *vs.* Mn stoichiometry is supposed to demonstrate superior electrochemical properties, resulting in improved performances when implemented in a real device. The CV tests carried out on the crystallized films showed an electrochemical response consistent with current knowledge of the electrochemistry of MnO_x-based materials, and emphasized a major impact of the film synthesis conditions. In conjunction with *ex situ* characterization measurements on aged samples and following the approach developed in [81], such CV measurements complemented by microscopic and spectroscopic analyses highlight a complex redox behaviour in aqueous electrolyte containing both Zn^{2+} and Mn^{2+}, which may involve multiple simultaneous processes such as Zn^{2+} insertion/extraction, H^+ insertion/extraction, ZHS precipitation/dissolution, and MnO_x deposition. Further electrochemical studies, combined with *in situ* characterization and analytical techniques capable of jointly yielding structural and chemical-state information, such as XAFS, will be undertaken in the near future, to fully elucidate the electrochemical mechanisms of the different ZMO films – in particular disentangling insertion and surface phase formation processes – to optimize their structure in view of the achievement and stabilization of high-capacity performance in real-life AZIBs.

Data availability

Data will be made available from the corresponding author upon reasonable request.

CRediT authorship contribution statement

Andrea Macrelli: Conceptualization, Methodology, Validation, Formal analysis, Investigation, Visualization, Writing – original draft, Writing – review & editing. **Marco Olivieri:** Formal analysis, Investigation. **Alessio Lamperti:** Methodology, Investigation, Resources, Writing – review & editing. **Valeria Russo:** Methodology, Supervision, Writing – review & editing. **Benedetto Bozzini:** Conceptualization, Methodology, Formal analysis, Resources, Writing – review & editing, Supervision. **Marco Menegazzo:** Methodology, Resources. **Gianlorenzo Bussetti:** Methodology, Resources. **Carlo S. Casari:** Conceptualization, Writing – review & editing, Supervision. **Andrea Li Bassi:** Conceptualization, Writing – review & editing, Supervision.

Declaration of Competing Interest

The authors declare that they have no known competing financial interests or personal relationships that could have appeared to influence the work reported in this paper.

Acknowledgments

The PhD scholarship of Andrea Macrelli and part of this research study pertain to the *Energy for Motion* project of the Department of Energy of Politecnico di Milano, funded by the Italian Ministry of University and Research (MIUR) through the Department of Excellence grant 2018 – 2022. A. Li Bassi, V. Russo and C.S. Casari acknowledge funding from the project PNRR - Partenariati estesi - "NEST - Network 4 Energy Sustainable Transition" - PE0000021.

Supplementary materials

Supplementary material associated with this article can be found, in the online version, at doi:10.1016/j.electacta.2023.141909.

References

[1] X. Jia, C. Liu, Z.G. Neale, J. Yang, G. Cao, Active materials for aqueous zinc ion batteries: synthesis, crystal structure, morphology, and electrochemistry, Chem. Rev. 120 (2020) 7795–7866, https://doi.org/10.1021/acs.chemrev.9b00628.
[2] T. Zhou, L. Zhu, L. Xie, Q. Han, X. Yang, L. Chen, G. Wang, X. Cao, Cathode materials for aqueous zinc-ion batteries: a mini review, J. Colloid Interface Sci. 605 (2022) 828–850, https://doi.org/10.1016/j.jcis.2021.07.138.
[3] L. Wang, J. Zheng, Recent advances in cathode materials of rechargeable aqueous zinc-ion batteries, Mater. Today Adv. 7 (2020), 1000782, https://doi.org/10.1016/j.mtadv.2020.100078.

[4] N. Wang, H. Wan, J. Duan, X. Wang, L. Tao, J. Zhang, H. Wang, A review of zinc-based battery from alkaline to acid, Mater. Today Adv. 11 (2021), 100149, https://doi.org/10.1016/j.mtadv.2021.100149.

[5] N. Borchers, S. Clark, B. Horstmann, K. Jayasayee, M. Juel, P. Stevens, Innovative zinc-based batteries, J. Power Sources 484 (2021), 229309, https://doi.org/10.1016/j.jpowsour.2020.229309.

[6] L.E. Blanc, D. Kundu, L.F. Nazar, Scientific challenges for the implementation of Zn-ion batteries, Joule 4 (2020) 771–799, https://doi.org/10.1016/j.joule.2020.03.002.

[7] V.P.H. Huy, L.T. Hieu, J. Hur, Zn metal anodes for Zn-ion batteries in mild aqueous electrolytes: challenges and strategies, Nanomaterials 11 (2021) 2746, https://doi.org/10.3390/nano11102746.

[8] C. Li, X. Xie, S. Liang, J. Zhou, Issues and future perspective on zinc metal anode for rechargeable aqueous zinc-ion batteries, Energy Environ. Mater. 3 (2020) 146–159, https://doi.org/10.1002/eem2.12067.

[9] Y. Geng, L. Pan, Z. Peng, Z. Sun, H. Lin, C. Mao, L. Wang, L. Dai, H. Liu, K. Pan, X. Wu, Q. Zhang, Z. He, Electrolyte additive engineering for aqueous Zn ion batteries, Energy Storage Mater. 51 (2022) 733–755, https://doi.org/10.1016/j.ensm.2022.07.017.

[10] N. Guo, W. Huo, X. Dong, Z. Sun, Y. Lu, X. Wu, L. Dai, L. Wang, H. Lin, H. Liu, H. Liang, Z. He, Q. Zhang, A review on 3D zinc anodes for zinc ion batteries, Small Methods 6 (2022), 2200597, https://doi.org/10.1002/smtd.202200597.

[11] T. Wang, C. Li, X. Xie, B. Lu, Z. He, S. Liang, J. Zhou, Anode materials for aqueous zinc ion batteries: mechanisms, properties, and perspectives, ACS Nano 14 (2020) 16321–16347, https://doi.org/10.1021/acsnano.0c07041.

[12] H. Li, L. Ma, C. Han, Z. Wang, Z. Liu, Z. Tang, C. Zhi, Advanced rechargeable zinc-based batteries: recent progress and future perspectives, Nano Energy 62 (2019) 550–587, https://doi.org/10.1016/j.nanoen.2019.05.059.

[13] B. Tang, L. Shan, S. Liang, J. Zhou, Issues and opportunities facing aqueous zinc-ion batteries, Energy Environ. Sci. 12 (2019) 3288–3304, https://doi.org/10.1039/c9ee02526j.

[14] M. Song, H. Tan, D. Chao, H.J. Fan, Recent advances in Zn-ion batteries, Adv. Funct. Mater. 28 (2018), 1802564, https://doi.org/10.1002/adfm.201802564.

[15] X. Guo, J. Zhou, C. Bai, X. Li, G. Fang, S. Liang, Zn/MnO_2 battery chemistry with dissolution-deposition mechanism, Mater. Today Energy 16 (2020), 100396, https://doi.org/10.1016/j.mtener.2020.100396.

[16] B. Lee, C.S. Yoon, H.R. Lee, K.Y. Chung, B.W. Cho, S.H. Oh, Electrochemically-induced reversible transition from the tunneled to layered polymorphs of manganese dioxide, Sci. Rep. 4 (2014) 6066, https://doi.org/10.1038/srep06066.

[17] W. Sun, F. Wang, S. Hou, C. Yang, X. Fan, Z. Ma, T. Gao, F. Han, R. Hu, M. Zhu, C. Wang, Zn/MnO_2 battery chemistry with H^+ and Zn^{2+} coinsertion, J. Am. Chem. Soc. 139 (2017) 9775–9778, https://doi.org/10.1021/jacs.7b04471.

[18] L. Li, T.K.A. Hoang, J. Zhi, M. Han, S. Li, P. Chen, Functioning mechanism of the secondary aqueous Zn-β-MnO_2 battery, ACS Appl. Mater. Interfaces 12 (2020) 12834–12846, https://doi.org/10.1021/acsami.9b22758.

[19] M.H. Alfaruqi, V. Mathew, J. Gim, S. Kim, J. Song, J.P. Baboo, S.H. Choi, J. Kim, Electrochemically induced structural transformation in a γ-MnO_2 cathode of a high capacity zinc-ion battery system, Chem. Mater. 27 (2015) 3609–3620, https://doi.org/10.1021/cm504717p.

[20] M.H. Alfaruqi, S. Islam, D.Y. Putro, V. Mathew, S. Kim, J. Jo, S. Kim, Y.K. Sun, K. Kim, J. Kim, Structural transformation and electrochemical study of layered MnO_2 in rechargeable aqueous zinc-ion battery, Electrochim. Acta 276 (2018) 1–11, https://doi.org/10.1016/j.electacta.2018.04.139.

[21] V. Mathew, B. Sambandam, S. Kim, S. Kim, S. Park, S. Lee, M.H. Alfaruqi, V. Soundharrajan, S. Islam, D.Y. Putro, J.Y. Hwang, Y.K. Sun, J. Kim, Manganese and vanadium oxide cathodes for aqueous rechargeable zinc-ion batteries: a focused view on performance, mechanism, and developments, ACS Energy Lett. 5 (2020) 2376–2400, https://doi.org/10.1021/acsenergylett.0c00740.

[22] W. Zhang, C. Zuo, C. Tang, W. Tang, B. Lan, X. Fu, S. Dong, P. Luo, The current developments and perspectives of V_2O_5 as cathode for rechargeable aqueous zinc-ion batteries, Energy Technol. 9 (2021), 2000789, https://doi.org/10.1002/ente.202000789.

[23] S. Liu, L. Kang, J.M. Kim, Y.T. Chun, J. Zhang, S.C. Jun, Recent advances in vanadium-based aqueous rechargeable zinc-ion batteries, Adv. Energy Mater. 10 (2020), https://doi.org/10.1002/aenm.202000477.

[24] G. Zampardi, F. La Mantia, Prussian blue analogues as aqueous Zn-ion batteries electrodes: current challenges and future perspectives, Curr. Opin. Electrochem. 21 (2020) 84–92, https://doi.org/10.1016/j.coelec.2020.01.014.

[25] H. Cui, T. Wang, Z. Huang, G. Liang, Z. Chen, A. Chen, D. Wang, Q. Yang, H. Hong, J. Fan, C. Zhi, High-voltage organic cathodes for zinc-ion batteries through electron cloud and solvation structure regulation, Angew. Chem. Int. Ed. 61 (2022), e202203453, https://doi.org/10.1002/anie.202203453.

[26] S. Xu, M. Sun, Q. Wang, C. Wang, Recent progress in organic electrodes for zinc-ion batteries, J. Semicond. 41 (2020), 091704, https://doi.org/10.1088/1674-4926/41/9/091704.

[27] J. Wang, J.G. Wang, H. Liu, Z. You, C. Wei, F. Kang, Electrochemical activation of commercial MnO microsized particles for high-performance aqueous zinc-ion batteries, J. Power Sources 438 (2019), 226951, https://doi.org/10.1016/j.jpowsour.2019.226951.

[28] C. Zhu, G. Fang, S. Liang, Z. Chen, Z. Wang, J. Ma, H. Wang, B. Tang, X. Zheng, J. Zhou, Electrochemically induced cationic defect in MnO intercalation cathode for aqueous zinc-ion battery, Energy Storage Mater. 24 (2020) 394–401, https://doi.org/10.1016/j.ensm.2019.07.030.

[29] M. Sun, D.S. Li, Y.F. Wang, W.L. Liu, M.M. Ren, F.G. Kong, S.J. Wang, Y.Z. Guo, Y. M. Liu, Mn_3O_4@NC composite nanorods as a cathode for rechargeable aqueous Zn-ion batteries, ChemElectroChem 6 (2019) 2510–2516, https://doi.org/10.1002/celc.201900376.

[30] J. Hao, J. Mou, J. Zhang, L. Dong, W. Liu, C. Xu, F. Kang, Electrochemically induced spinel-layered phase transition of Mn_3O_4 in high performance neutral aqueous rechargeable zinc battery, Electrochim. Acta 259 (2018) 170–178, https://doi.org/10.1016/j.electacta.2017.10.166.

[31] H. Jiang, X. Ji, Counter-ion insertion of chloride in Mn_3O_4 as cathode for dual-ion batteries: a new mechanism of electrosynthesis for reversible anion storage, Carbon Energy 2 (2020) 437–442, https://doi.org/10.1002/cey2.37.

[32] C. Zhu, G. Fang, J. Zhou, J. Guo, Z. Wang, C. Wang, J. Li, Y. Tang, S. Liang, Binder-free stainless steel@Mn_3O_4 nanoflower composite: a high-activity aqueous zinc-ion battery cathode with high-capacity and long-cycle-life, J. Mater. Chem. A 6 (2018) 9677–9683, https://doi.org/10.1039/c8ta01198b.

[33] D. Feng, T.N. Gao, L. Zhang, B. Guo, S. Song, Z.A. Qiao, S. Dai, Boosting high-rate zinc-storage performance by the rational design of Mn_2O_3 nanoporous architecture cathode, Nano-Micro Lett. 12 (2020) 14, https://doi.org/10.1007/s40820-019-0351-4.

[34] Y. Ma, Y. Ma, T. Diemant, K. Cao, X. Liu, U. Kaiser, R.J. Behm, A. Varzi, S. Passerini, Unveiling the intricate intercalation mechanism in manganese sesquioxide as positive electrode in aqueous Zn-metal battery, Adv. Energy Mater. 11 (2021), 2100962, https://doi.org/10.1002/aenm.202100962.

[35] B. Jiang, C. Xu, C. Wu, L. Dong, J. Li, F. Kang, Manganese sesquioxide as cathode material for multivalent zinc ion battery with high capacity and long cycle life, Electrochim. Acta 229 (2017) 422–428, https://doi.org/10.1016/j.electacta.2017.01.163.

[36] Y. Cai, R. Chua, S. Huang, H. Ren, M. Srinivasan, Amorphous manganese dioxide with the enhanced pseudocapacitive performance for aqueous rechargeable zinc-ion battery, Chem. Eng. J. 396 (2020), 125221, https://doi.org/10.1016/j.cej.2020.125221.

[37] Y. Wu, J. Fee, Z. Tobin, A. Shirazi-Amin, P. Kerns, S. Dissanayake, A. Mirich, S. L. Suib, Amorphous manganese oxides: an approach for reversible aqueous zinc-ion batteries, ACS Appl. Energy Mater. 3 (2020) 1627–1633, https://doi.org/10.1021/acsaem.9b02119.

[38] M.H. Alfaruqi, J. Gim, S. Kim, J. Song, J. Jo, S. Kim, V. Mathew, J. Kim, Enhanced reversible divalent zinc storage in a structurally stable α-MnO_2 nanorod electrode, J. Power Sources 288 (2015) 320–327, https://doi.org/10.1016/j.jpowsour.2015.04.140.

[39] B. Lee, H.R. Lee, H. Kim, K.Y. Chung, B.W. Cho, S.H. Oh, Elucidating the intercalation mechanism of zinc ions into α-MnO_2 for rechargeable zinc batteries, Chem. Commun. 51 (2015) 9265–9268, https://doi.org/10.1039/c5cc02585k.

[40] S. Islam, M.H. Alfaruqi, V. Mathew, J. Song, S. Kim, S. Kim, J. Jo, J.P. Baboo, D. T. Pham, D.Y. Putro, Y.K. Sun, J. Kim, Facile synthesis and the exploration of the zinc storage mechanism of β-MnO_2 nanorods with exposed (101) planes as a novel cathode material for high performance eco-friendly zinc-ion batteries, J. Mater. Chem. A 5 (2017) 23299–23309, https://doi.org/10.1039/c7ta07170a.

[41] M.H. Alfaruqi, J. Gim, S. Kim, J. Song, D.T. Pham, J. Jo, Z. Xiu, V. Mathew, J. Kim, A layered δ-MnO_2 nanoflake cathode with high zinc-storage capacities for eco-friendly battery applications, Electrochem. Commun. 60 (2015) 121–125, https://doi.org/10.1016/j.elecom.2015.08.019.

[42] C. Guo, H. Liu, J. Li, Z. Hou, J. Liang, J. Zhou, Y. Zhu, Y. Qian, Ultrathin δ-MnO_2 nanosheets as cathode for aqueous rechargeable zinc ion battery, Electrochim. Acta 304 (2019) 370–377, https://doi.org/10.1016/j.electacta.2019.03.008.

[43] D. Chao, W. Zhou, C. Ye, Q. Zhang, Y. Chen, L. Gu, K. Davey, S. Qiao, An electrolytic Zn–MnO_2 battery for high-voltage and scalable energy storage, Angew. Chem. Int. Ed. 58 (2019) 7823–7828, https://doi.org/10.1002/anie.201904174.

[44] C. Yuan, Y. Zhang, Y. Pan, X. Liu, G. Wang, D. Cao, Investigation of the intercalation of polyvalent cations (Mg^{2+}, Zn^{2+}) into λ-MnO_2 for rechargeable aqueous battery, Electrochim. Acta 116 (2014) 404–412, https://doi.org/10.1016/j.electacta.2013.11.090.

[45] J. Lee, J.B. Ju, W. il Cho, B.W. Cho, S.H. Oh, Todorokite-type MnO_2 as a zinc-ion intercalating material, Electrochim. Acta 112 (2013) 138–143, https://doi.org/10.1016/j.electacta.2013.08.136.

[46] L. Nádherný, M. Maryško, D. Sedmidubský, C. Martin, Structural and magnetic properties of $Zn_xMn_{3-x}O_4$ spinels, J. Magn. Magn. Mater. 413 (2016) 89–96, https://doi.org/10.1016/j.jmmm.2016.04.029.

[47] M. Peiteado, S. Sturm, A.C. Caballero, D. Makovec, $Mn_{3-x}Zn_xO_4$ spinel phases in the Zn-Mn-O system, Acta Mater. 56 (2008) 4028–4035, https://doi.org/10.1016/j.actamat.2008.04.024.

[48] S. Guillemet-Fritsch, C. Chanel, J. Sarrias, S. Bayonne, A. Rousset, X. Alcobe, M. L. Martinez Sarriòn, Structure, thermal stability and electrical properties of zinc manganites, Solid State Ion. 128 (2000) 233–242, https://doi.org/10.1016/S0167-2738(99)00340-9.

[49] L. Malavasi, P. Galinetto, M.C. Mozzati, C.B. Azzoni, G. Flor, Raman spectroscopy of AMn_2O_4 (A = Mn, Mg and Zn) spinels, Phys. Chem. Chem. Phys. 4 (2002) 3876–3880, https://doi.org/10.1039/b203520k.

[50] A. Baby, B. Senthilkumar, P. Barpanda, Low-cost rapid template-free synthesis of nanoscale zinc spinels for energy storage and electrocatalytic applications, ACS Appl. Energy Mater. 2 (2019) 3211–3219, https://doi.org/10.1021/acsaem.9b00054.

[51] N. Zhang, F. Cheng, Y. Liu, Q. Zhao, K. Lei, C. Chen, X. Liu, J. Chen, Cation-deficient spinel $ZnMn_2O_4$ cathode in $Zn(CF_3SO_3)_2$ electrolyte for rechargeable aqueous Zn-ion battery, J. Am. Chem. Soc. 138 (2016) 12894–12901, https://doi.org/10.1021/jacs.6b05958.

[52] J.C. Knight, S. Therese, A. Manthiram, Chemical extraction of Zn from $ZnMn_2O_4$-based spinels, J. Mater. Chem. A 3 (2015) 21077–21082, https://doi.org/10.1039/c5ta06482a.

[53] K. Cai, S.-h. Luo, J. Feng, J. Wang, Y. Zhan, Q. Wang, Y. Zhang, X. Liu, Recent advances on spinel zinc manganate cathode materials for zinc-ion batteries, Chem. Rec. 22 (2022), e202100169, https://doi.org/10.1002/tcr.202100169.

[54] H. Zhang, J. Wang, Q. Liu, W. He, Z. Lai, X. Zhang, M. Yu, Y. Tong, X. Lu, Extracting oxygen anions from $ZnMn_2O_4$: robust cathode for flexible all-solid-state Zn-ion batteries, Energy Storage Mater. 21 (2019) 154–161, https://doi.org/10.1016/j.ensm.2018.12.019.

[55] J.W. Lee, S.D. Seo, D.W. Kim, Comparative study on ternary spinel cathode Zn–Mn–O microspheres for aqueous rechargeable zinc-ion batteries, J. Alloy. Compd. 800 (2019) 478–482, https://doi.org/10.1016/j.jallcom.2019.06.051.

[56] T.H. Wu, W.Y. Liang, Reduced intercalation energy barrier by rich structural water in spinel $ZnMn_2O_4$ for high-rate zinc-ion batteries, ACS Appl. Mater. Interfaces 13 (2021) 23822–23832, https://doi.org/10.1021/acsami.1c05150.

[57] S. Islam, M.H. Alfaruqi, D.Y. Putro, S. Park, S. Kim, S. Lee, M.S. Ahmed, V. Mathew, Y.K. Sun, J.Y. Hwang, J. Kim, *In situ* oriented Mn deficient $ZnMn_2O_4$@C nanoarchitecture for durable rechargeable aqueous zinc-ion batteries, Adv. Sci. 8 (2021), 2002636, https://doi.org/10.1002/advs.202002636.

[58] S. Wang, S. Zhang, X. Chen, G. Yuan, B. Wang, J. Bai, H. Wang, G. Wang, Double-shell zinc manganate hollow microspheres embedded in carbon networks as cathode materials for high-performance aqueous zinc-ion batteries, J. Colloid Interface Sci. 580 (2020) 528–539, https://doi.org/10.1016/j.jcis.2020.07.053.

[59] X. Wu, Y. Xiang, Q. Peng, X. Wu, Y. Li, F. Tang, R. Song, Z. Liu, Z. He, X. Wu, Green-low-cost rechargeable aqueous zinc-ion batteries using hollow porous spinel $ZnMn_2O_4$ as the cathode material, J. Mater. Chem. A 5 (2017) 17990–17997, https://doi.org/10.1039/c7ta00100b.

[60] L. Chen, Z. Yang, H. Qin, X. Zeng, J. Meng, H. Chen, Graphene-wrapped hollow $ZnMn_2O_4$ microspheres for high-performance cathode materials of aqueous zinc ion batteries, Electrochim. Acta 317 (2019) 155–163, https://doi.org/10.1016/j.electacta.2019.05.147.

[61] L. Chen, Z. Yang, H. Qin, X. Zeng, J. Meng, Advanced electrochemical performance of $ZnMn_2O_4$/N-doped graphene hybrid as cathode material for zinc ion battery, J. Power Sources 425 (2019) 162–169, https://doi.org/10.1016/j.jpowsour.2019.04.010.

[62] M.B. Sassin, M.E. Helms, J.F. Parker, C.N. Chervin, R.H. Deblock, J.S. Ko, D. R. Rolison, J.W. Long, Elucidating zinc-ion battery mechanisms in freestanding carbon electrode architectures decorated with nanocrystalline $ZnMn_2O_4$, Mater. Adv. 2 (2021) 2730–2738, https://doi.org/10.1039/d1ma00159k.

[63] Z. Yao, D. Cai, Z. Cui, Q. Wang, H. Zhan, Strongly coupled zinc manganate nanodots and graphene composite as an advanced cathode material for aqueous zinc ion batteries, Ceram. Int. 46 (2020) 11237–11245, https://doi.org/10.1016/j.ceramint.2020.01.148.

[64] C. Yang, M. Han, H. Yan, F. Li, M. Shi, L. Zhao, *In-situ* probing phase evolution and electrochemical mechanism of $ZnMn_2O_4$ nanoparticles anchored on porous carbon polyhedrons in high-performance aqueous Zn-ion batteries, J. Power Sources 452 (2020), 227826, https://doi.org/10.1016/j.jpowsour.2020.227826.

[65] S. Deng, Z. Tie, F. Yue, H. Cao, M. Yao, Z. Niu, Rational design of $ZnMn_2O_4$ quantum dots in a carbon framework for durable aqueous zinc-ion batteries, Angew. Chem. Int. Ed. 61 (2022), e202115877, https://doi.org/10.1002/anie.202115877.

[66] Y. Tao, Z. Li, L. Tang, X. Pu, T. Cao, D. Cheng, Q. Xu, H. Liu, Y.G. Wang, Y. Xia, Nickel and cobalt co-substituted spinel $ZnMn_2O_4$@N-rGO for increased capacity and stability as a cathode material for rechargeable aqueous zinc-ion battery, Electrochim. Acta 331 (2020), 135296, https://doi.org/10.1016/j.electacta.2019.135296.

[67] K. Cai, S. Luo, J. Cong, K. Li, S. Yan, P. Hou, Q. Wang, Y. Zhang, X. Liu, X. Lei, Synthesis and optimization of $ZnMn_2O_4$ cathode material for zinc-ion battery by citric acid sol-gel method, J. Electrochem. Soc. 169 (2022), 030531, https://doi.org/10.1149/1945-7111/ac5baa.

[68] T. Shao, Y. Zhang, T. Cao, Y. Yang, Z. Li, H. Liu, Y. Wang, X. Yongyao, Structural regulation of $ZnMn_2O_4$ cathode material by K, Fe-double doping to improve its rate and cycling stability for rechargeable aqueous zinc-based batteries, Chem. Eng. J. 431 (2022), 133735, https://doi.org/10.1016/j.cej.2021.133735.

[69] S. Yang, M. Zhang, X. Wu, X. Wu, F. Zeng, Y. Li, S. Duan, D. Fan, Y. Yang, X. Wu, The excellent electrochemical performances of $ZnMn_2O_4/Mn_2O_3$: the composite cathode material for potential aqueous zinc ion batteries, J. Electroanal. Chem. 832 (2019) 69–74, https://doi.org/10.1016/j.jelechem.2018.10.051.

[70] Y. Zeng, Y. Wang, Q. Jin, Z. Pei, D. Luan, X. Zhang, X.W. Lou, Rationally designed Mn_2O_3-$ZnMn_2O_4$ hollow heterostructures from metal-organic frameworks for stable Zn-ion storage, Angew. Chem. Int. Ed. 60 (2021) 25793–25798, https://doi.org/10.1002/anie.202113487.

[71] S.C. Ma, M. Sun, S.X. Wang, D.S. Li, W.L. Liu, M.M. Ren, F.G. Kong, S.J. Wang, Y. M. Xia, Zinc manganate/manganic oxide bi-component nanorod as excellent cathode for zinc-ion battery, Scr. Mater. 194 (2021), 113707, https://doi.org/10.1016/j.scriptamat.2020.113707.

[72] M. Shi, B. Wang, Y. Shen, J. Jiang, W. Zhu, Y. Su, M. Narayanasamy, S. Angaiah, C. Yan, Q. Peng, 3D assembly of MXene-stabilized spinel $ZnMn_2O_4$ for highly durable aqueous zinc-ion batteries, Chem. Eng. J. 399 (2020), 125627, https://doi.org/10.1016/j.cej.2020.125627.

[73] W. Qiu, H. Xiao, H. Feng, Z. Lin, H. Gao, W. He, X. Lu, Defect modulation of $ZnMn_2O_4$ nanotube arrays as high-rate and durable cathode for flexible quasi-solid-state zinc ion battery, Chem. Eng. J. 422 (2021), 129890, https://doi.org/10.1016/j.cej.2021.129890.

[74] T.H. Wu, C.C. Huang, S.L. Cheng, C.C. Lin, Expanded spinel $Zn_xMn_2O_4$ induced by electrochemical activation of glucose-mediated manganese oxide for stable cycle performance in zinc-ion batteries, J. Colloid Interface Sci. 617 (2022) 274–283, https://doi.org/10.1016/j.jcis.2022.03.017.

[75] V. Soundharrajan, B. Sambandam, S. Kim, S. Islam, J. Jo, S. Kim, V. Mathew, Y. kook Sun, J. Kim, The dominant role of Mn^{2+} additive on the electrochemical reaction in $ZnMn_2O_4$ cathode for aqueous zinc-ion batteries, Energy Storage Mater. 28 (2020) 407–417, https://doi.org/10.1016/j.ensm.2019.12.021.

[76] C.M. Julien, A. Mauger, Pulsed laser deposited films for microbatteries, Coatings 9 (2019) 386, https://doi.org/10.3390/coatings9060386.

[77] M. Fenech, N. Sharma, Pulsed laser deposition-based thin film microbatteries, Chem. Asian. J. 15 (2020) 1829–1847, https://doi.org/10.1002/asia.202000384.

[78] L. Indrizzi, N. Ohannessian, D. Pergolesi, T. Lippert, E. Gilardi, Pulsed laser deposition as a tool for the development of all solid-state microbatteries, Helv. Chim. Acta 104 (2021), e2000203, https://doi.org/10.1002/hlca.202000203.

[79] P.R. Willmott, J.R. Huber, Pulsed laser vaporization and deposition, Rev. Mod. Phys. 72 (2000) 315–328, https://doi.org/10.1103/RevModPhys.72.315.

[80] C.S. Casari, A. Li Bassi, Pulsed laser deposition of nanostructured oxides: from clusters to functional films, in: W.T. Arkin (Ed.), Advances in Laser and Optics Research, Vol. 7, Ch. 2, Nova Science Publishers, Inc., Hauppauge (NY), USA, 2011, pp. 65–100.

[81] F. Rossi, E. Marini, M. Boniardi, A. Casaroli, A. Li Bassi, A. Macrelli, C. Mele, B. Bozzini, What happens to MnO_2 when it comes in contact with Zn^{2+}? An electrochemical study in aid of Zn/MnO_2-based rechargeable batteries, Energy Technol. 10 (2022), 2200084, https://doi.org/10.1002/ente.202200084.

[82] S. Åsbrink, A. Waśkowska, L. Gerward, J. Staun Olsen, E. Talik, High-pressure phase transition and properties of spinel $ZnMn_2O_4$, Phys. Rev. B 60 (1999) 12651–12656, https://doi.org/10.1103/PhysRevB.60.12651.

[83] R. Matarrese, I. Nova, A. Li Bassi, C.S. Casari, V. Russo, S. Palmas, Preparation and optimization of TiO_2 photoanodes fabricated by pulsed laser deposition for photoelectrochemical water splitting, J. Solid State Electrochem. 21 (2017) 3139–3154, https://doi.org/10.1007/s10008-017-3639-7.

[84] P. Gondoni, P. Mazzolini, V. Russo, M. Diani, M. Amati, L. Gregoratti, V. De Renzi, G.C. Gazzadi, J. Martí-Rujas, A. Li Bassi, C.S. Casari, Tuning electrical properties of hierarchically assembled Al-doped ZnO nanoforests by room temperature pulsed laser deposition, Thin Solid Films 594 (2015) 12–17, https://doi.org/10.1016/j.tsf.2015.09.066.

[85] A. Bailini, F. Di Fonzo, M. Fusi, C.S. Casari, A. Li Bassi, V. Russo, A. Baserga, C. E. Bottani, Pulsed laser deposition of tungsten and tungsten oxide thin films with tailored structure at the nano- and mesoscale, Appl. Surf. Sci. 253 (2007) 8130–8135, https://doi.org/10.1016/j.apsusc.2007.02.145.

[86] B.R. Bricchi, L. Mascaretti, S. Garattoni, M. Mazza, M. Ghidelli, A. Naldoni, A. Li Bassi, Nanoporous titanium (oxy)nitride films as broadband solar absorbers, ACS Appl. Mater. Interfaces 14 (2022) 18453–18463, https://doi.org/10.1021/acsami.2c01185.

[87] F. Di Fonzo, C.S. Casari, V. Russo, M.F. Brunella, A. Li Bassi, C.E. Bottani, Hierarchically organized nanostructured TiO_2 for photocatalysis applications, Nanotechnology 20 (2009), 015604, https://doi.org/10.1088/0957-4484/20/1/015604.

[88] H. Li, B. Song, W.J. Wang, X.L. Chen, Facile synthesis, thermal, magnetic, Raman characterizations of spinel structure $ZnMn_2O_4$, Mater. Chem. Phys. 130 (2011) 39–44, https://doi.org/10.1016/j.matchemphys.2011.04.072.

[89] K. Samanta, S. Dussan, R.S. Katiyar, P. Bhattacharya, Structural and optical properties of nanocrystalline $Zn_{1-x}Mn_xO$, Appl. Phys. Lett. 90 (2007), 261903, https://doi.org/10.1063/1.2751593.

[90] C.M. Julien, M. Massot, C. Poinsignon, Lattice vibrations of manganese oxides: part I. Periodic structures, Spectrochim. Acta A Mol. Biomol. Spectrosc. 60 (2004) 689–700, https://doi.org/10.1016/S1386-1425(03)00279-8.

[91] M. Tortosa, F.J. Manjón, M. Mollar, B. Marí, ZnO-based spinels grown by electrodeposition, J. Phys. Chem. Solids 73 (2012) 1111–1115, https://doi.org/10.1016/j.jpcs.2012.04.002.

[92] J. Zuo, C. Xu, Y. Liu, Y. Qian, Crystallite size effects on the Raman spectra of Mn_3O_4, NanoStructured Mater. 10 (1998) 1331–1335, https://doi.org/10.1016/S0965-9773(99)00002-1.

[93] A.V. Chichagov, D.A. Varlamov, R.A. Dilanyan, T.N. Dokina, N.A. Drozhzhina, O. L. Samokhvalova, T.V. Ushakovskaya, MINCRYST: a crystallographic database for minerals, local and network (WWW) versions, Crystallogr. Rep. 46 (2001) 876–879, https://doi.org/10.1134/1.1405882.

[94] WWW-MINCRYST. Crystallographic and crystallochemical database for minerals and their structural analogues. http://database.iem.ac.ru/mincryst (accessed July 29, 2022).

[95] G.K. Williamson, W.H. Hall, X-ray line broadening from filed aluminium and wolfram, Acta Metall. 1 (1953) 22–31, https://doi.org/10.1016/0001-6160(53)90006-6.

[96] D. Nath, F. Singh, R. Das, X-ray diffraction analysis by Williamson-Hall, Halder-Wagner and size-strain plot methods of CdSe nanoparticles - a comparative study, Mater. Chem. Phys. 239 (2020), 122021, https://doi.org/10.1016/j.matchemphys.2019.122021.

[97] S. Bernardini, F. Bellatreccia, A. Casanova Municchia, G. Della Ventura, A. Sodo, Raman spectra of natural manganese oxides, J. Raman Spectrosc. 50 (2019) 873–888, https://doi.org/10.1002/jrs.5583.

[98] J. Yang, J. Cao, Y. Peng, W. Yang, S. Barg, Z. Liu, I.A. Kinloch, M.A. Bissett, R.A. W. Dryfe, Unravelling the mechanism of rechargeable aqueous Zn–MnO_2 batteries: implementation of charging process by electrodeposition of MnO_2, ChemSusChem 13 (2020) 4103–4110, https://doi.org/10.1002/cssc.202001216.